The importance of being homogeneous – on the influence of illumination inhomogeneity on AIMS images

Arndt C. Dürr[a*], Karsten Bubke[a], Martin Sczyrba[a], Samuel Angonin[b]

[a]Advanced Mask Technology Center (AMTC), Rähnitzer Alle 9, 01109 Dresden (Germany)
[b]UTBM Université de Technologie Belfort-Montbéliard, 90010 Belfort-CEDEX, France

ABSTRACT

Defect disposition and qualification with stepper simulating AIMS^{TM} tools on advanced masks of the 90 nm node and below is key to match the customer's expectations for "defect free" masks, i.e. masks containing only non-printing design variations. For defect dispositioning usually printability studies are carried out using the same illumination settings at the AIMS^{TM} tool as later on at the steppers in the wafer fab. These studies then establish an AIMS^{TM} criterion (e.g., CD variation or transmission deviation) a structure deviation must not exceed. For ever more advanced technologies the accessible process window gets smaller and thus more and more complex apertures have to be used to allow for a still suitable contrast and reliable printing of the patterns. This results in more time-consuming printability studies and tighter AIMS^{TM} specs. Simulations of the printing of mask defects could potentially help to decrease the amount of time for printability studies and also the time for defect disposition in the production. However, usually simulations in their first approximation do not account for effects such as flare, aberrations or illumination inhomogeneities of the AIMS^{TM} tool. This makes it difficult to derive the AIMS^{TM} criterion by simulations. In this paper we show that a homogeneous aperture illumination is crucial for the image contrast and the defect disposition. We present a method to characterize the pupil illumination and investigate the impact of illumination inhomogeneities on various structures and their orientation employing two different aperture types. The experimental results are compared to simulations with both homogeneous illumination and the real illumination distribution. It turns out that for correct simulation predictions on experimental results it is important to provide the correct illumination distribution to the simulations.

Keywords: Keywords: AIMS, Defect disposition, Lithography Simulation, Aerial imaging, 193nm lithography, Printability, Optical imaging, Mask, Reticle

1. INTRODUCTION

As modern lithography steps deeper into the regime of low k1, the requirements on pattern quality and allowed defect sizes for photomasks become tighter. In a maskshop the defect qualification on a photomask is usually performed using an AIMS^{TM} tool, which simulates the aerial image of a photomask under illumination settings that the mask will later be exposed within the wafer process.[1–5] Usually, for any new technology node and material type extensive printability studies are performed in collaboration between maskhouse and customer to find an appropriate AIMS^{TM} defect dispositioning criterion telling whether a defective site will later-on print on the wafer and therefore needs to be repaired or not.[6–10]

Currently, a lot of effort is put on the simulation of defect printing to reduce the time consumption of printing studies and also to disposition defects in production.[11–14] However, the matching between AIMS^{TM} results and simulations is often unsatisfactory since the imperfections of the AIMS^{TM} optics are normally not included in simulations (e.g., flare, aberrations, cross-talk, inhomogeneous illumination).[15,16] This discrepancy between simulation and measurement is exemplified in the upper part of Figure 1 on a lines and spaces (referred to as l&s hereafter) pattern for annular illumination[†]. In addition, the lower part of Figure 1 shows the orientation dependence of the measured contrast of the same lines and spaces pattern, which can be attributed to the

*Further author information: (Send correspondence to Arndt C. Dürr)
Arndt C. Dürr: E-mail: Arndt.Duerr@amtc-dresden.com, Telephone: +49 (0) 351 4048 268

[†]Note, that also the simulations exhibit an uncertainty due to the unknown side-wall angle, not perfectly known mask parameters and numerical limitations.

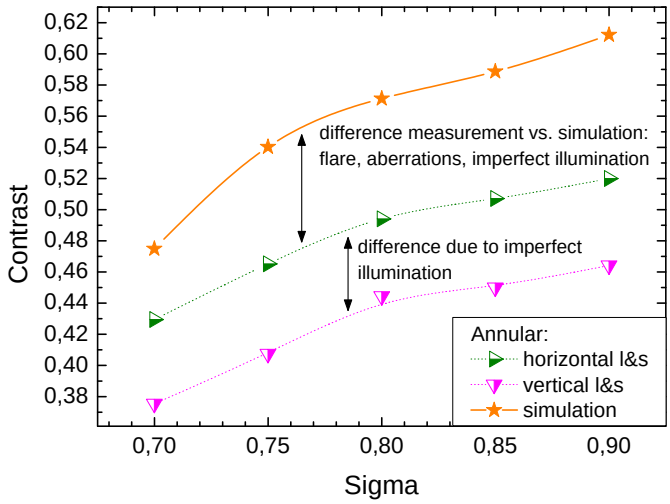

Figure 1. Difference in contrast between AIMS^{TM} measurements and a simulation for a lines and spaces pattern illuminated with an annular aperture, $\sigma_{in}/\sigma_{out} = 0.66$, $NA = 0.75$ and variable σ_{out}. Triangles represent measurements for the l&s pattern in horizontal and vertical orientation, respectively. The lines are guides to the eye.

inhomogeneous illumination. To allow for upcoming tighter specs for defect disposition in the production the homogeneity of the illumination plays a key role. Aside a small tool variability it is mandatory to account for the remaining illumination inhomogeneities to arrive at a better match between simulation and measurements.

In this paper we systematically investigate the influence of inhomogeneous aperture illumination on AIMS^{TM} results and show how to improve the matching between AIMS^{TM} results and simulations when the inhomogeneities are taken into account in the simulations. We further study the influence of a parameterized model of the pupil illumination on the simulation results.

2. INFLUENCE OF PUPIL IMPERFECTIONS ON DEFECT QUALIFICATION

2.1. Defect Qualification using an AIMS-tool

Figure 2 shows a typical image of a defective site in a vertically oriented lines and spaces (l&s) pattern. For the evaluation of the measurement data the AIMS^{TM} transmission at the defective defect site is compared to a defect free site in the following way (see also Fig. 2): The light intensity of the maximum I_{DefMax} at the defect is evaluated with the help of the AIMS^{TM} software. Also an average light intensity of the defect free maxima is taken (I_{RefMax}). The intensity values for defect minimum I_{DefMin} and the average reference minima I_{RefMin} are determined in the same way.

The differences of light intensity at a defective site in the defect maximum ($MaxTrans$) and in the defect minimum ($MinTrans$) as well as the contrast C of the pattern are calculated using the following formulas:

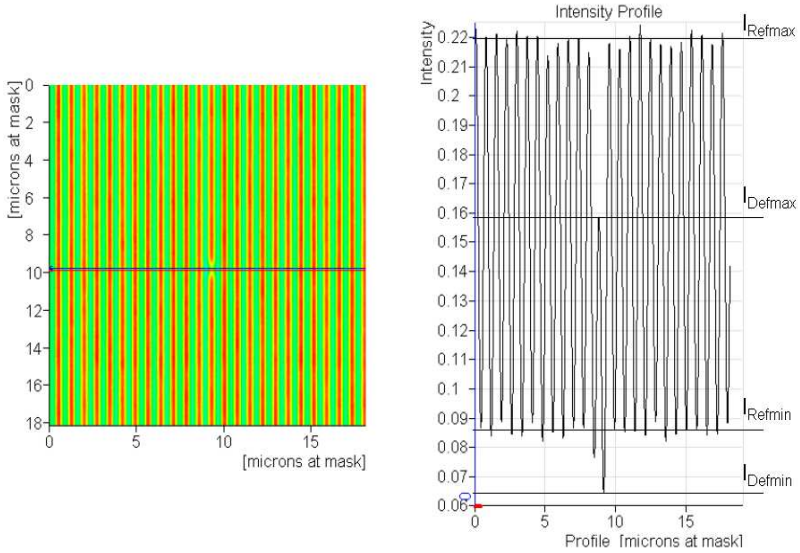

Figure 2. AIMS$^{\mathrm{TM}}$ image of a l&s structure and cross-section along the line in the left-hand-side image. On the right hand side the intensity oscillations of the structure along the cross-section are seen. The intensities I_{RefMax}, I_{DefMax}, I_{RefMin}, and I_{DefMin} needed for the AIMS$^{\mathrm{TM}}$ evaluation are shown.

$$MaxTrans = \left(1 - \frac{I_{DefMax}}{I_{RefMax}}\right) \times 100\% \tag{1}$$

$$MinTrans = \frac{I_{DefMin} - I_{RefMin}}{I_{RefMax} - I_{RefMin}} \times 100\% \tag{2}$$

$$C = \frac{I_{RefMax} - I_{RefMin}}{I_{RefMax} + I_{RefMin}} \ . \tag{3}$$

2.2. Imaging of patterns

Figure 3 shows schematically the main concepts of imaging for a l&s pattern with quasar illumination. From left to right the imaging process is sketched: light from a light source with a given angular distribution [on-axis vs. off-axis: in the black circle (representing the NA) the light source's shape, size, and its position with respect to the NA is indicated] and intensity I_0 is incident onto the pattern to be imaged and is diffracted in the pattern's Fourier-components (right-hand side) with diffraction efficiencies $\eta_0 \ldots \eta_n$ where η_m is the intensity of diffraction order m, I_m normalized to I_0:

$$\eta_m = I_m / I_0 \ . \tag{4}$$

Imaging of the pattern is only possible if at least 2 diffraction orders interfere.

For an on-axis point-source and a sufficient tight l&s-pattern [see Fig. 3(a)] only the 0^{th} order falls in the NA and thus the pattern will not be resolved on the wafer or in the AIMS$^{\mathrm{TM}}$-tool.[17–19] Still using a point-source, however, from an off-axis position [see Fig. 3(b)] the refraction pattern is simply moved and two orders fall into

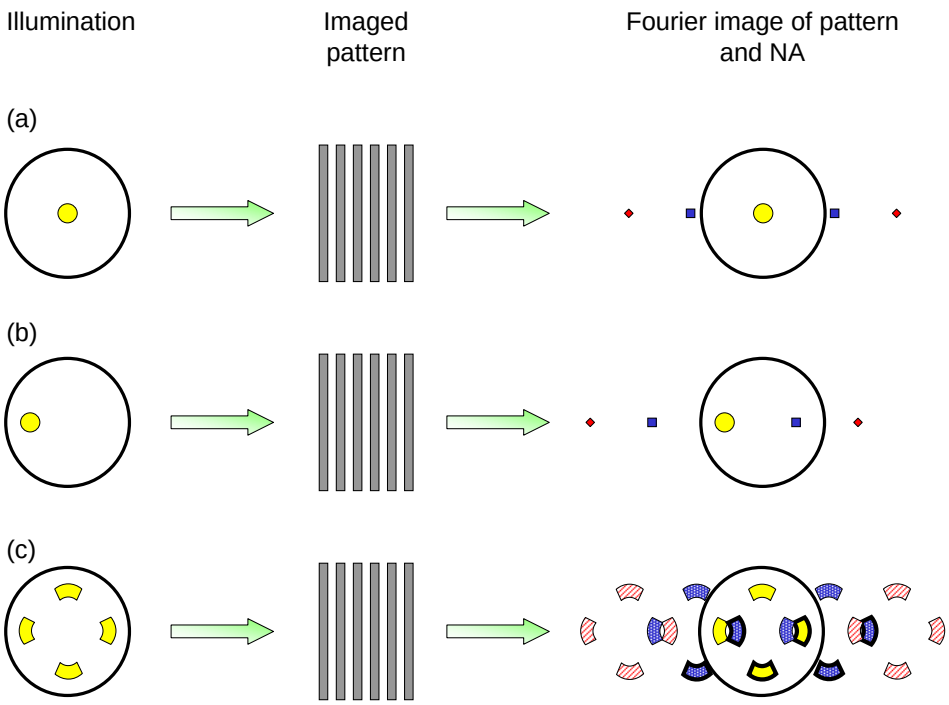

Figure 3. Imaging of a l&s pattern under various illumination settings. On the left-hand side position, size and shape of the illumination source are displayed. The black circle represents the size of the NA. In the middle, the l&s-pattern to be imaged is seen. On the right-hand side, the NA (black circle) and a schematic for the Fourier-spectrum as a result of the employed illumination are shown: yellow symbols/shapes [(a) and (b): $\circ$] $\equiv 0^{th}$ diffraction order with efficiency η_0, blue symbols/shapes [(a) and (b): $\square$] $\equiv \pm 1^{st}$ diffraction order with efficiency η_1, red symbols/shapes [(a) and (b): $\diamond$] $\equiv \pm 2^{nd}$ diffraction order with efficiency η_2. (a) illumination with on-axis point source, (b) illumination with off-axis point source, (c) illumination with quasar aperture.

the NA enabling pattern imaging. Figure 3(c) shows a real illumination aperture (quasar type) which can be considered to be composed of many point-sources and the resulting diffraction pattern. Again, the diffraction pattern of each point-source within the aperture is simply moved in the imaging plane with respect to the case of the on-axis point-source of Fig. 3(a) resulting in quasar-like diffraction patterns. A closer inspection of the pattern shows that for each horizontal pole of the aperture two diffraction orders fall within the NA whereas for the vertical poles only the 0^{th} order falls within the NA – for the "right" and the "bottom" pole this is indicated by the thick black lines surrounding the 0^{th} and 1^{st} diffraction order, respectively. Note, that the imaging for structures with a more continuous diffraction pattern (e.g., defects) is not that critically dependent on optimized illumination conditions since in this case intrinsically more than only the 0^{th} diffraction order falls into the NA.

2.3. Influence of Pupil Imperfections on Imaging

For the investigation of inhomogeneous pupil (i.e., aperture) illumination it is helpful to characterize the pupil illumination by a simple parameterization: "ellipticity" (E), "pole balance X" (PBX, along its East-West axis), and "pole balance Y" (PBY, along its North-South axis). As indicated in Fig. 4, the parameters are defined by the integrated intensities in 4 sectors (I_N , I_E , I_S , I_W) of the respective apertures as

$$E = \frac{(I_N + I_S) - (I_W + I_E)}{(I_N + I_S) + (I_W + I_S)} \tag{5}$$

$$PBX = \frac{I_W - I_E}{I_W + I_S} \tag{6}$$

$$PBY = \frac{I_N - I_S}{I_N + I_S} \ . \tag{7}$$

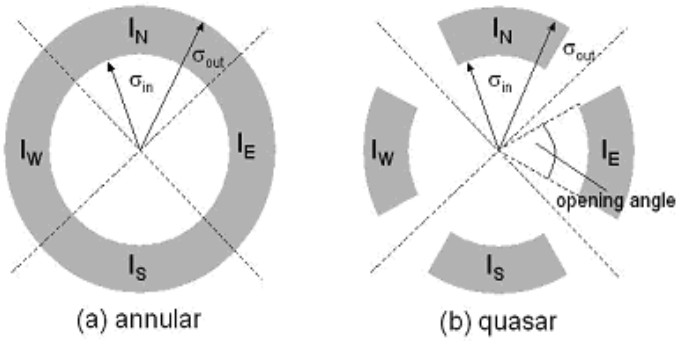

Figure 4. Definition of relevant parameter for (a) annular illumination and (b) quasar illumination.

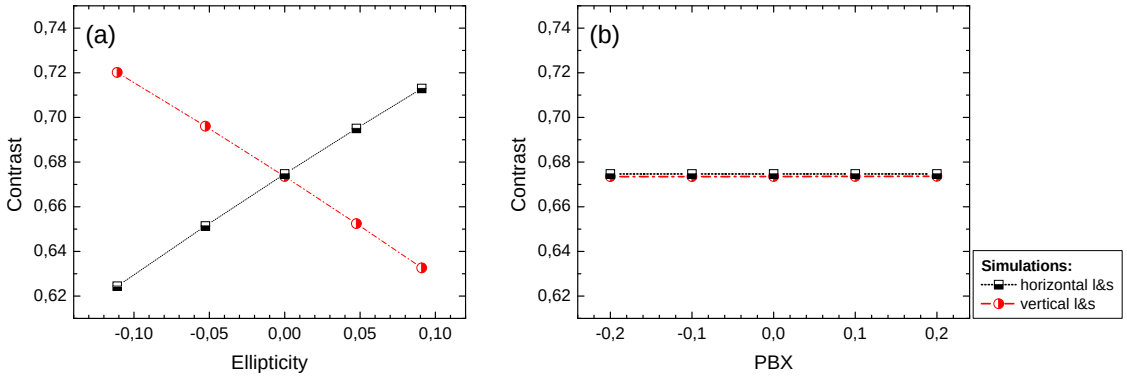

Figure 5. (a) Contrast of dense lines and spaces in vertical and horizontal direction using quasar illumination, 60° opening angle, $\sigma_{in}/\sigma_{out} = 0.78$, $\sigma_{out} = 0.85$, $NA = 0.75$. (a) as a function of ellipticity at constant $PBX = PBY = 0$, (b) as a function of PBX at constant ellipticity $E = PBY = 0$.

To give an impression of the influence of an inhomogeneous pupil illumination we consider the simple case of a dense l&s-pattern aligned with the North-South axis as shown on the left-hand side of Fig. 2 and further assume an optimized illumination with a quasar aperture.

As pointed out in Section 2.2 [see Fig. 3(c)] for small pitches only light of the West-East poles contribute to imaging (with the interference of their 0^{th} and 1^{st} diffraction order) whereas light from the South-North poles

raises solely the intensity level and hence decreases the contrast (only the 0^{th} order falls in the NA). Under these assumptions the contrast of lines in vertical direction can be written as,

$$C_{||} = \frac{2(I_W + I_E)\sqrt{\eta_0\eta_1}}{(I_W + I_E)(\eta_0 + \eta_1) + (I_N + I_S)\eta_0} \tag{8}$$

$$= \frac{2\sqrt{\eta_0\eta_1}}{\frac{2}{1-E}\eta_0 + \eta_1} \quad , \tag{9}$$

where E is the ellipticity defined in Eq. 5 and η_0 and η_1 are the efficiencies in the 0^{th} and 1^{st} diffraction order as defined in Eq. 4. For horizontally oriented l&s-patterns a similar equation could be derived. Eq. 9 shows that the influence of the individual incoming light intensities on C is summarized in E and thus C is only dependent on the ellipticity E and the intensities in the 0^{th} and 1^{st} diffraction orders. Assuming $\eta_0 \approx \eta_1$ yields $C \approx 0.66$ for the discussed quasar aperture. For an X-disar aperture (i.e., $I_N = I_S = 0$) and again $\eta_0 \approx \eta_1$, Eq. 9 results in $C \approx 1$.

Figure 5(a) displays the Contrast C of a horizontal and vertical l&s-pattern as a function of the ellipticity E at $PBX = PBY = 0$ for quasar illumination with $\sigma_{in}/\sigma_{out} = 0.78$, opening angle 60° and $NA = 0.75$, $\sigma_{out} = 0.85$. The result matches to Eq. 9 and demonstrate an inhomogeneous intensity distribution in the pupil will lead to a varying contrast depending on the direction of lines on the mask, i.e., that vertical l&s-patterns exhibit a larger C for $E < 0$ (i.e., increased W-E-illumination) and horizontal l&s-patterns exhibit a larger C for $E > 0$. Figure 5(b) shows that C does not depend on PBX for $E = PBY = 0$ for the investigated quasar aperture. C is also independent on PBY (data not shown). This is in accordance with Eq. 9: here, C is only dependent on E.

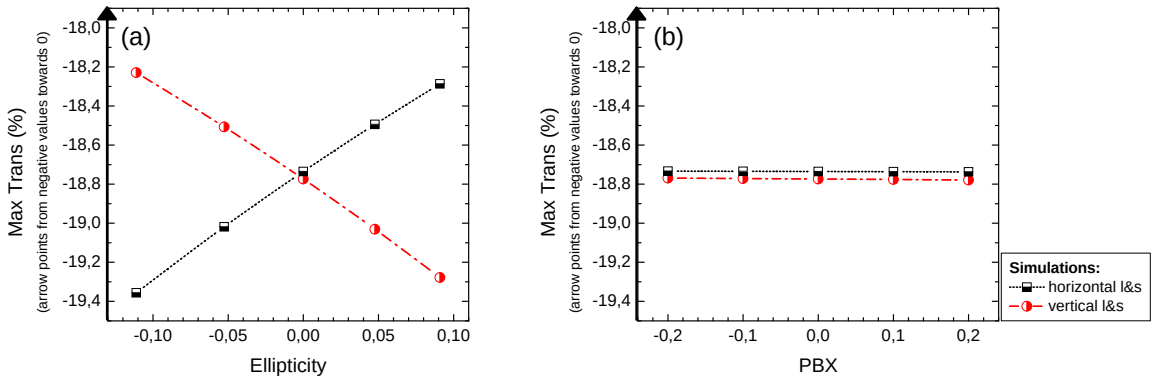

Figure 6. Simulation of $MaxTrans$ of typical dark defect using quasar illumination, 60° opening angle, $\sigma_{in}/\sigma_{out} = 0.78$, $\sigma_{out} = 0.85$, $NA = 0.75$ (a) as a function of ellipticity at constant $PBX = PBY = 0$, (b) as a function of PBX at constant ellipticity $E = PBY = 0$.

To study the effect of pupil inhomogeneities on defect evaluation a simulation with varying ellipticity at constant $PBX = PBY = 0$ and with varying PBX at constant $E = PBY = 0$, respectively, was carried out for $MaxTrans$ of a typical dark defect. The result for varying E is illustrated in Fig. 6(a). Note, that for the case of quasar illumination also $MaxTrans$ does not depend on PBX [see Fig. 6(b)]. Further simulations (not shown here) demonstrated that the printing of defects is neither affected by PBY. These results demonstrate that defect printing is largely dependent on the contrast of the main feature (see also the considerations at the end of Section 2.2).

3. EXPERIMENTAL

3.1. Masks and illumination settings

In the present study the masks were imaged with an AIMS^{TM}fab 193SE system. In Fig. 7 examples of intensity distributions in the pupil are shown for an annular and a quasar illumination. Nonuniformities in the pupil can clearly be observed.

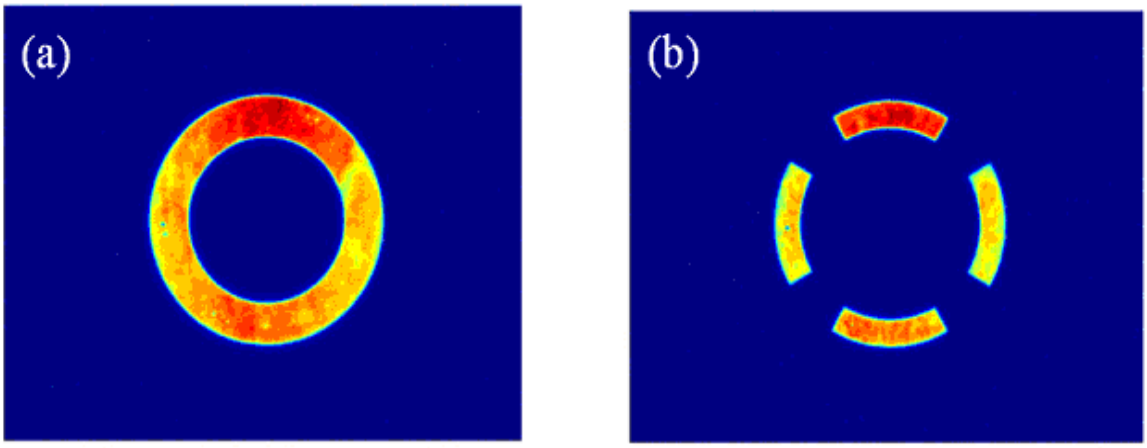

Figure 7. Intensity distribution of the two apertures used in this study: (a) Annular 66%, (b) Quasar 78% 60°.

Two different masks with l&S-patterns were used for the experiments. As stated above, for a comparison of simulations and measurements one has to keep in mind that there are a number of imperfections of the optical systems influencing the AIMS^{TM} -image. These are aside the pupil inhomogeneity, e.g., flare, cross-talk or lens aberrations, where the former two are considered to be the major effects.[15,16] To distinguish between these effects from those originating from the pupil inhomogeneity, AIMS^{TM} -images of the same structure were acquired in both vertical and horizontal direction. As flare and crosstalk should be less direction dependent, a comparison between both images gives a good indication of the influence of pupil illumination inhomogeneity.

(A) To determine the printing behavior of a model type dark defect (Fig. 8) a mask with programmed defects in an 88 nm (on wafer level) l&s pattern (i.e., 352 nm lines and 352 nm spaces on masks level) on MoSi 193 nm material was used. For this investigation we used the apertures listed in Table 1. For each aperture images were taken at a constant $NA = 0.75$ with varying sigma (σ_{out} = 0.7 / 0.75 / 0.8 / 0.85 / 0.9). This mask is referred to as "Mask A" hereafter.

(B) In addition, a mask with l&s-structures of constant pitch but varying duty cycle (i.e., the ratio between line and spaces) on MoSi 193 nm was used with a quasar aperture at constant $NA = 0.75$ and constant $\sigma_{out} = 0.85$. This mask is referred to as "Mask B" hereafter.

3.2. Simulations

All simulations were performed using the optical lithography simulator SOLID-C allowing for the incorporation of arbitrary pupil shapes defined by the user. For simulations with real sources the actual pupil image was acquired on the AIMS^{TM} -tool and then converted with an in-house conversion tool into a format readable by SOLID-C. For top-hat simulations the predefined pupil shapes were used. All l&s-patterns were simulated in

Table 1. Aperture types used in this study.

aperture name	ratio σ_{in}/σ_{out}	opening angle [°]
Annular 66%	0.66	–
Quasar 78%/60°	0.78	60

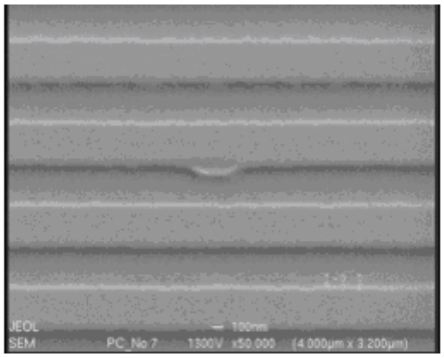

Figure 8. Dark defect of mask A used for the AIMS^{TM} imaging in this study

vertical and horizontal orientation, respectively, to make the simulations comparable to the measured data. A common systematic error in simulations is the shape of the defect used in the numerics. In all calculations the defect was assumed to be rectangular in shape. Furthermore, the Kirchhoff-approximation was used, i.e., the mask was assumed to be infinitely thin.

4. RESULTS AND DISCUSSION

4.1. Measurement and simulation of the contrast of horizontal and vertical l&s patterns

Figure 9(a) shows the results for the contrast C of mask A for annular and quasar illumination in 0° and 90° orientation, respectively. The solid lines depict the contrast obtained by simulations with a perfectly homogeneous aperture illumination. The simulations clearly show that for all sigma values $C_{quasar} > C_{annular}$. This holds also true for the measurements if the same orientation of the l&s pattern is compared. However, for $\sigma \leq 0.85$ the contrast for annular illumination on the l&s pattern in horizontal orientation clearly exceeds the contrast of the same pattern in vertical orientation illuminated through the quasar aperture. Taking into account the inhomogeneous illumination of the apertures (see Fig. 7) with $E \neq 0$ can easily be explained by Eq. 9: since $E > 0$ the contrast for a vertical l&s-pattern and quasar illumination is reduced. On the other hand, the contrast for a horizontally oriented l&s-pattern is enhanced for $E > 0$ and for a certain E then even an annular pupil can provide a higher contrast than quasar illumination of the same pattern in vertical orientation (*n*ote, that Eq. 9 does not account for annular illumination!). The difference between the contrasts of the l&s pattern in horizontal and vertical orientation for a given aperture is almost constant over the investigated sigma-range. For annular illumination the difference is of the order of $\Delta C_{annular,meas} \approx 0.05$ whereas for quasar illumination $\Delta C_{quasar,meas} \approx 0.068$ is found.

The increase in contrast for increasing σ-values for annular apertures and the almost constant $C(\sigma)$ for quasar apertures can easily be explained with Fig. 3: for all investigated σ values the 1^{st} diffraction-order-patterns of the quasar aperture always fall completely in the NA. Decreasing of σ will eventually result in a shift of the 1^{st} diffraction order out of the NA and thus in a decrease of C. On the other hand, for the annular apertures imaging the given tight l&s-pattern, decreasing σ always leads to a shrinking of the 1^{st} order diffraction area in the NA and therefore of the interfering area. The remaining 0^{th} order counterparts remain in the NA but only contribute to the non-imaging intensity, hence a continuously decreasing C is observed.

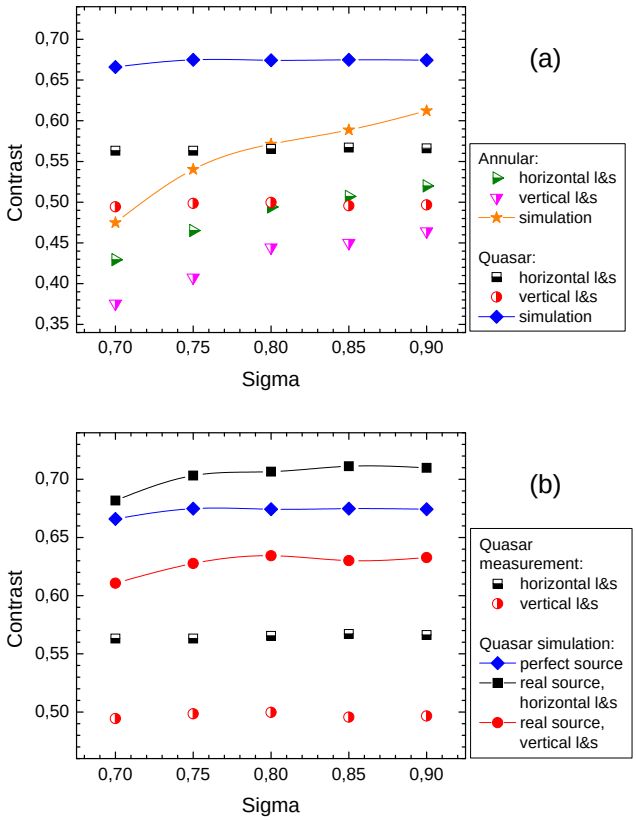

Figure 9. (a) Difference in contrast between AIMS^{TM} measurements with an annular and quasar aperture for a l&s pattern in vertical and horizontal orientation, respectively (half filled symbols). The solid lines represent contrast simulations for this l&s pattern assuming perfectly homogeneous illumination of the annular and quasar aperture. (b) Contrast measurements (half filled symbols) and contrast simulations (solid lines and full symbols) using a perfectly homogeneous (blue diamonds) and the real apertures for the l&s pattern in horizontal (black squares) and vertical orientation (red circles) imaged by a quasar aperture.

As a further step we investigated if it is possible to reflect the measurement results in the simulations. For this purpose we performed simulations on the l&s pattern in horizontal and vertical orientation using the real pupil intensity distribution as source of illumination. Since the results for annular and quasar illumination show a similar behavior we focus on quasar illumination for the rest of the paper. Figure 9(b) shows the results of these simulations as well as the measured contrast values. Additionally, the results of a simulation with a perfectly homogeneous aperture [see also Fig. 9(a)] are displayed. The spread in contrast of the real aperture simulations between the two orientations for the 5 investigated sigma values is almost constant and of the order of $\Delta C_{quasar,sim} \approx 0.075$ [$\Delta C_{annular,sim} \approx 0.048$, data not shown], well in accordance to the experimentally determined values. As expected, the simulated contrast curve for the perfectly homogenous illuminated pupil is laying between the two simulated curves derived with the real illumination distribution. The still existing difference between the measured data and the simulated data for the same orientation can be attributed to the above mentioned effects such as flare, crosstalk, aberrations, etc.[15, 16] which are characteristic for the hardware of any tool and are yet neither strongly reduced (as for e.g. in steppers) nor included in the simulations. The results emphasize - as long as illumination inhomogeneities exist in AIMS^{TM} tools - the importance of the use of the real aperture intensity distribution in the simulations to arrive at a decent simulation-measurement matching.

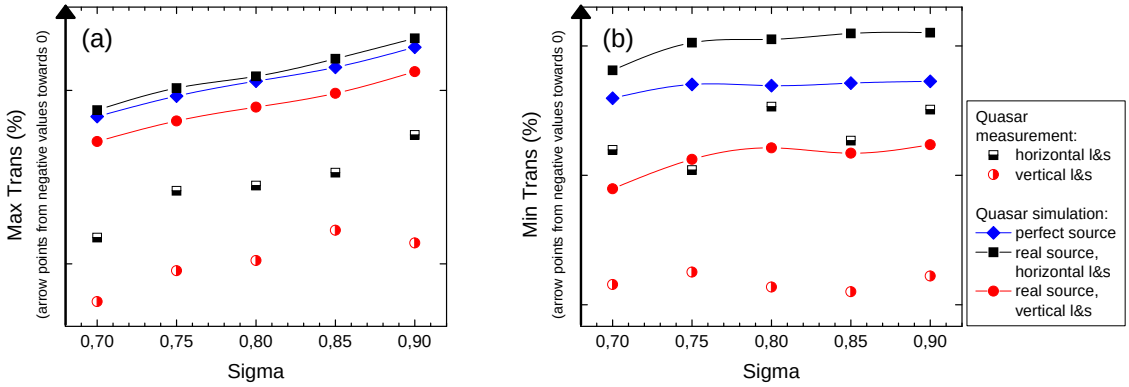

Figure 10. Transmission loss of a dark defect in a l&s pattern imaged with quasar illumination (see Fig. 7). Note that the y-axis points from negative values towards 0, i.e., the higher a data point lies on the y-axis the less is the transmission deviation with respect to a defect free structure. Half filled symbols represent measurement values for horizontal (black squares) and vertical (red circles) oriented structures. Solid lines with filled symbols depict simulations (perfect source: blue, diamonds; real source, horizontal structures: black, squares; real source, vertical structures: red circles). (a) $MaxTrans$ for measurements and simulations (b) $MinTrans$ for measurements and simulations.

4.2. Defect disposition: comparison of measurement and simulation for quasar illumination

Next, we investigated the influence of the illumination inhomogeneity on defect dispositioning. For this experiment a defective site (see Fig. 8) of mask A was measured and simulated (with perfectly homogeneous aperture and with the real intensity distributions of the aperture) in vertical and horizontal orientation, respectively. The intensity deviations at the defective site were calculated according to Eqs. 2 and 3. Figures 10(a) and 10(b) show the results for the defect's maximum and minimum, respectively. *Note*, that the y-axis of both plots points from negative values towards 0 since the defect is a dark defect, i.e., the higher a data point lies on the $MaxTrans$- or $MinTrans$-axis the closer it lies to zero deviation. Again, similar to the contrast measurements and simulations, an orientation dependence spread in $MaxTrans$ and $MinTrans$ is observed for both, measurements and simulations. For the employed aperture illuminations the transmission deviation is always smaller for horizontally oriented l&s patterns than for vertically oriented (i.e., the transmission-loss values lie higher on the y-axis). The simulations show that the curve for defect-transmission-loss using a perfectly homogeneous aperture lies between the two curves using the real intensity distributions. The simulated transmission-losses using real apertures have nearly the same differences between the two orientations ($\Delta MaxTrans_{sim}$ and $\Delta MinTrans_{sim}$) as the measured data ($\Delta MaxTrans_{meas}$ and $\Delta MinTrans_{meas}$) for all investigated sigma values. Figures 10(a) and 10(b) also show that the simulated defect deviations have less transmission deviation than the measured data (i.e. the $MaxTrans$ and $MinTrans$ values lie higher on the y-axis). Thus, it is obvious, that the defect transmission deviation anti-correlates with the contrast: the higher the contrast the less deviates the transmission at the defect site from a reference structure confirming also the considerations of Section 2 (Figs. 5 and 6).

As briefly discussed at the end of Section 2.2 this can be understood by the different Fourier-spectra of the l&s-pattern and the defect, respectively. The tight l&s-pattern with its only 2 diffraction orders contributing to imaging is critically dependent on optimized illumination conditions (homogeneous, centered) to obtain an optimum C. On the other hand, the contrast of a defect with its continuous diffraction spectrum is largely independent on shifts and inhomogeneities of the illumination. Thus, the larger the l&s-contrast the less is the *relative* effect of a defect on the pattern's imaging (and thus the smaller are $MaxTrans$ and $MinTrans$) and vice-versa.

These findings demonstrate that an inhomogeneous aperture illumination results in orientation dependent $MaxTrans$ and $MinTrans$ values and reduces - together with an intrinsic tool-variability when taking AIMS^{TM} images - the process window of defect qualification. Also it is shown that a proper simulation of AIMS^{TM} values requires real aperture illumination intensity distributions as input.

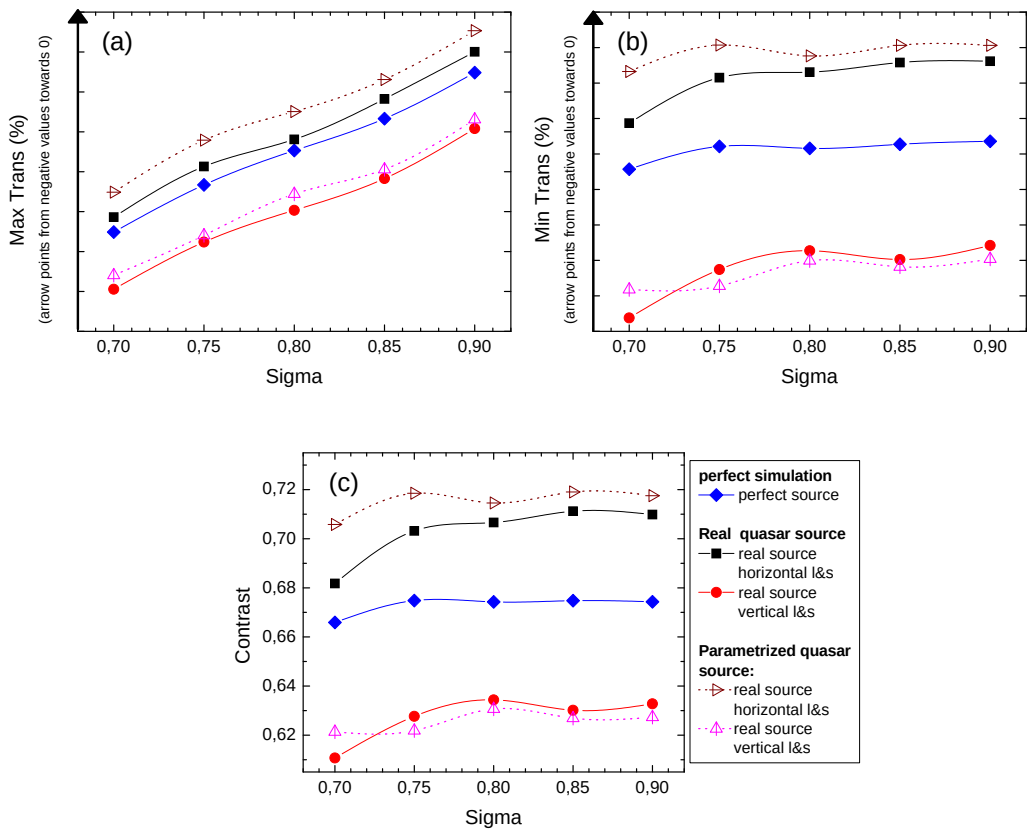

Figure 11. (a) - (c) Comparison of the simulated $MaxTrans$, $MinTrans$, and C for the already discussed horizontal and vertical l&s pattern. The Simulations were carried out using the real sources (solid lines) and the parameterized sources (dotted lines), respectively. Also the simulations employing a perfectly homogeneous source are displayed.

4.3. Comparison of simulations using real aperture images and parameterized aperture model

Even though the simulation of AIMS^{TM} images with the real intensity distribution is possible quite some effort is necessary to get started: the pupil image has to be saved and afterwards needs to be transformed into a suitable data-format for the SOLID-C software. This process is time and memory consuming and also could lead to mistakes during the image conversion. Furthermore, it is questionable to which extent the simulations are sensitive to short wavelength oscillations in the intensity distribution. In other words, the question arises if it is possible to represent the intensity distribution by a small set of parameters and how large the deviations between simulations with such a parameterized model on the one hand and simulations with the real sources on the other hand are. For the parameterization we used E, PBX, and PBY as defined in Eqs. 5-7.

Figures 11 (a)-(c) show that the simulations with parameterized sources are in excellent agreement with the real-source simulations for the vertical l&s pattern. Therefore, for the simulation of the horizontally oriented l&s pattern the matching between the two simulation approaches is not perfect. However, taking into account that the chosen parameterization is describing a whole aperture illumination intensity distribution by only 3 parameters the agreement is acceptable. It would be interesting for future studies to investigate the need of refinement in the parameterization to get a sufficient match. A possible application then would be to determine this parameter-set of the employed pupil directly during the mask set-up by the AIMS^{TM} software, incorporate them afterward directly in the simulation software and thus allow for a much more easy access to close-to-reality AIMS^{TM} simulations.

4.4. Investigation on lines and space patterns with different duty cycle and application of a simple flare model

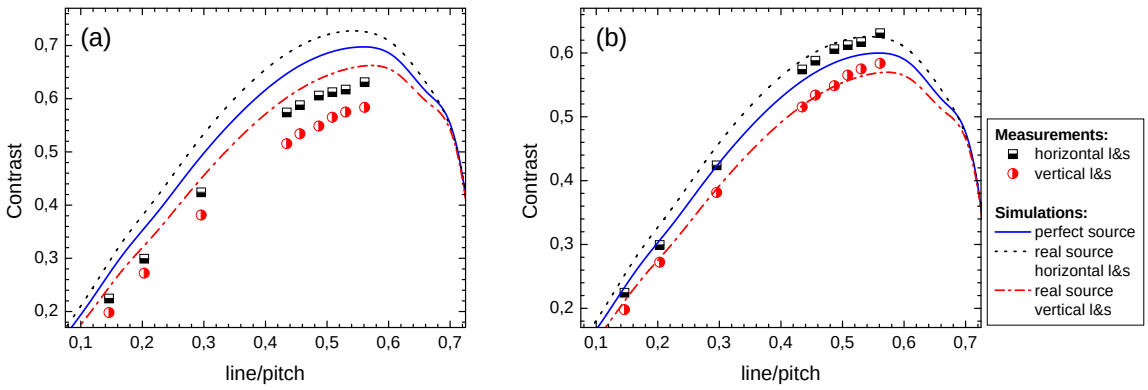

Figure 12. (a) Contrast for measurements on horizontally (half filled black squares) and vertically (half filled red circles) oriented l&s patterns, respectively, with varying duty cycle imaged with a quasar aperture. The lines represent simulations utilizing a perfectly homogeneous pupil (blue, solid) and the real sources for the horizontally (black, dotted) and vertically (dash-dotted, red) oriented l&s patterns, respectively. (b) same as (a) but after application of a linear flare factor of 0.86 to all 3 simulations.

Having established a simulation method which accounts for the pupil inhomogeneities and therefore makes a comparison between measurements and simulations more sound the question arises if – based on these results – it is possible to implement also a model for the remaining hardware-effects (flare, cross-talk, aberrations) into the simulations to get them into a real close match to the measurements.

This question was investigated on mask B by imaging of l&s structures with fixed pitch of 180 nm on wafer level but varying duty cycle (the ratio between line and pitch). The measurements were carried out with the quasar 78%/60° aperture at constant $NA = 0.75$ and $\sigma = 0.85$ for the l&s-patterns oriented first vertically and then horizontally.

Fig. 12(a) shows the results of measurements and simulations. As for the measurements and simulations before, the contrast of the l&s-pattern in vertical and horizontal direction shows a deviation which can be attributed to pupil imperfections. The simulated contrast is still larger than the measured contrast for the same orientation which is mainly due to flare and crosstalk.[16] Note the fairly constant offset between measurements and simulations for both orientations.

To account for the remaining hardware effects we incorporated a simple linear model to the simulation. Figure 12(b) displays the results: by multiplying the simulation data with 0.86 it is possible to bring simulations and measurements in a reasonable agreement. The applied factor implies that the hardware effects of the AIMS^{TM} tool and of the mask account for a contrast loss of $\approx 14\%$ compared to the simulations. However, it is shown, that implementing real aperture intensity distributions in the simulations are a mandatory step for a more realistic simulation-measurement matching and the foundation for more subtle flare-crosstalk models.

4.5. Discussion of simulation aspect

One aspect of the simulations with real apertures needs some attention. In the previous sections it was shown that using real aperture intensity distributions as input for the simulations considerably improved the significance of the simulated data. However, to acquire a real aperture image in the AIMS^{TM} tool a much shorter exposure time is used (ca. 20 ms) than for the measurement of a l&s-pattern (ca. 200-800 ms) in order to avoid camera damage since for the acquisition of images of the aperture the so-called “Bertrand-optic” has to be used in the AIMS^{TM}-tool. Thus, it might be possible that a single aperture “snapshot” is not representative for the intensity distribution being present during imaging the l&s-pattern. To investigate if there is a significant effect of the exposure time on the intensity distribution and hence on the simulations we measured the intensity of a pupil

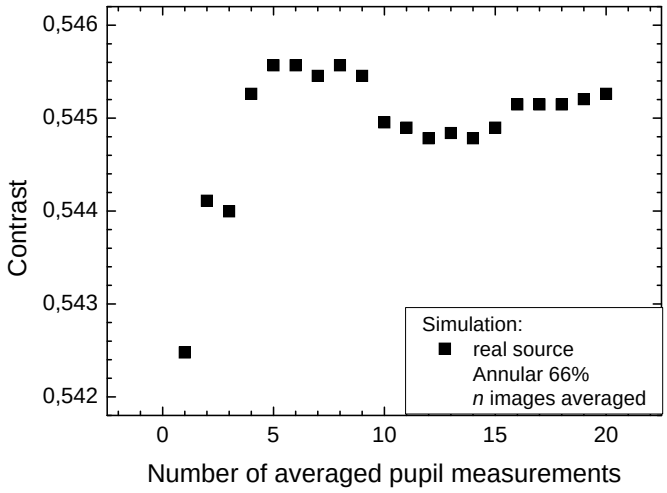

Figure 13. Simulated contrast for a l&s pattern as a function of an increasing number of real apertures averaged used as illumination source.

(annular 66%, NA= 0.75, $\sigma = 0.75$ several times in a series. Then, the contrast of the l&s-pattern of mask A was simulated as a function of an increasing number of aperture "snapshots" averaged, see Fig. 13. Up to 20 aperture "snapshots" were averaged amounting to a total exposure time of ca. 400 ms. The contrast increases for the first 4 pupil "snapshots" averaged from 0.5424 to 0.5452 and then stabilizes. This demonstrates that the difference in contrast is less than 0.7% between maximum and minimum contrast. Therefore, the averaging effect has been neglected in the other simulations.

5. SUMMARY AND CONCLUSIONS

In this paper we have shown at the example of two different l&s patterns imaged in an AIMS tool with an annular and a quasar aperture, respectively, that the intensity distribution of the aperture has a significant influence on contrast and defect printing of the imaged structure. For inhomogeneous illumination (in particular for an ellipticity $E \neq 0$) the measurement results are dependent on the orientation of the l&s-pattern (vertical vs. horizontal). A key result is that for a sound comparison of defect simulations (e.g., for defect dispositioning or to derive AIMS criteria from simulated printability studies) to real AIMS measurements it is mandatory to simulate any structure with the real illumination intensity distribution. It was further shown, that implementing the aperture intensity distribution in the simulation software (SOLID-C) by a few parameter model leads to an acceptable match with simulations using the real aperture intensity distribution results – it will be an interesting aspect for further studies how much refinement to the parameter model is needed to exactly get a perfect match to the real aperture simulations. Also, it could be shown that using real aperture images for the simulations with a small exposure time of ca. 20 ms for the acquisition of an aperture image with the AIMS [compared to the exposure time for taking an image of the l&s-pattern (ca. 200-800 ms)] does not reduce the simulation quality significantly. After the separation of the illumination inhomogeneity effects in the simulations still remaining differences between real-aperture simulations and measurements are – except of aberration effects – independent of orientation and can therefore be attributed to flare, cross-talk. A simple flare model (not accounting for space-frequency dependence) was applied to the simulation data for a mask with varying duty-cycle leading to an acceptable match with the measurements on the same mask. The present results lay the foundations for the development of a more subtle flare-model providing a better simulation-measurement match. Finally, to arrive at reliable and reproducible defect dispositioning in mask-shops, the results emphasize for the AIMS aperture illumination the importance of being homogeneous.

ACKNOWLEDGMENTS

The authors wish to thank Marcel Einert, Stefan Hinzdorf, and Falk Hoffmann for their help in taking AIMS images.

REFERENCES

1. R. A. Budd, J. L. Staples, D. B. Dove, "New tool for phase-shift mask evaluation: the stepper equipment aerial image measurement system–AIMS", Proc. SPIE Vol. 2087, pp. 162-171, 1994.
2. R. M. Martino, R. A. Ferguson, R. A. Budd, J. L. Staples, L. W. Liebmann, A. F. Molless, D. B. Dove, J. T. Weed, "Application of the aerial image measurement system (AIMS)^{TM} to the analysis of binary mask imaging and resolution enhancement techniques", Proc. SPIE Vol. 2197, pp. 573-584, 1994.
3. S. A. Rizvi, N. A. Diachun, "The AIMS tool: its potentials, applications, and issues", Proc. SPIE Vol. 3546, pp. 494-497, 1998.
4. R. L. Gordon, D. G. Flagello, M. McCallum, "Deducing aerial image behavior from AIMS data", Proc. SPIE Vol. 4000, pp. 734-743, 2000.
5. C. E. Tabery, C. A. Spence, "Evaluation of 3D alternating PSM structures using mask topography simulation, and AIMS at $\lambda = 193$ nm ", Proc. SPIE Vol. 4346, pp. 429-440, 2001.
6. V. Philipsen, R. M. Jonckheere, S. Kohlpoth, C. M. Friedrich, J. A. Torres, "Printability of hard and soft defects in 193-nm lithography", Proc. SPIE Vol. 4764, pp. 95-111, 2002.
7. V. Philipsen, R. M. Jonckheere , "Extended Defect Printability Study for 100nm Design Rule using 193 nm Lithography ", Proc. SPIE Vol. 4889, pp. 509-519, 2002.
8. S. Akima, T. Komizo, S. Kawakita, Y. Kodera, T. Narita, K. Ishikawa, "Phase defect printability and mask inspection capability of 65-nm technology node Alt-PSM for ArF lithography", Proc. SPIE Vol. 5567, pp. 23-35, 2004.
9. K. Eggers, K. Gutjahr, M. Peikert, D. Rutzinger, R. Ludwig, M. Kaiser, A. Dürr, J. Heumann , "Defect printability and inspectability of halftone masks for the 90nm and 70nm node", Proc. SPIE Vol. 5835, pp. 273-281, 2005.
10. J. Heumann, J. Schramm, A. Birnstein, K. T. Park, T. Witte, N. Morgana, M. Hennig, R. Pforr, J. Thiele, N. Schmidt, C. Aquino, "Defect printability and inspectability of Cr-less phase-shift masks for the 70nm node", Proc. SPIE Vol. 5754, pp. 1022-1028, 2005.
11. D. J. Bald, S. Munir, B. Lieberman, W. H. Howard, C. A. Mack , "PRIMADONNA: a system for automated defect disposition of production masks using wafer lithography simulation", Proc. SPIE Vol. 4889, pp. 263-270, 2002.
12. A. B. Nhiev, J. Hickethier, H. Zhou, T. A. Hutchinson, W. Howard, M. Ahmadian, "A study of defect measurement techniques and corresponding effects on the lithographic process window for a 193-nm EPSM photomask", Proc. SPIE Vol. 5256, pp. 1120-1129, 2003.
13. A. Erdmann, "Process optimization using lithography simulation", Proc. SPIE Vol. 5401, pp. 22-36, 2004.
14. A. Erdmann, "Mask modeling in the low k1 and ultrahigh NA regime: phase and polarization effects", Proc. SPIE Vol. 5835, pp. 69-81, 2005.
15. R. Koehle, W. Dettmann, M. Verbeek, "Fourier analysis of AIMS images for mask characterization", Proc. SPIE Vol. 5130, pp. 545-554, 2003.
16. S. Teuber, I. Higashikawa, J.-P. Urbach, C. M. Schilz, R. Koehle, A. M. Zibold, "First results from AIMS beta tool for 157-nm lithography", Proc. SPIE Vol. 5377, pp. 1648-1657, 2004.
17. A. K.-K. Wong, *Resolution Enhancement Techniques in Optical Lithography*, Tutorial texts in optical engineering, Vol. TT47, SPIE Press, Bellingham, Washington, 2001.
18. J. S. Petersen, "Optical proximity strategies for desensitizing lens aberrations", Proc. SPIE Vol. 4404, pp. 254-265, 2001.
19. R. Köhle, M. Hennig, R. Pforr, K. Bubke, M. Sczyrba, A. C. Dürr, "Aerial image based mask defect detection in dense array structures", Proc. SPIE Vol. 5853, pp. 953-964, 2005.